

Ⓞ Precipitation, Temperature, and Teleconnection Signals across the Combined North American, Monsoon Asia, and Old World Drought Atlases

SEUNG H. BAEK,^{a,b} JASON E. SMERDON,^a SLOAN COATS,^{c,d} A. PARK WILLIAMS,^a BENJAMIN I. COOK,^{a,e}
EDWARD R. COOK,^a AND RICHARD SEAGER^a

^a *Lamont-Doherty Earth Observatory, Columbia University, Palisades, New York*

^b *Department of Earth and Environmental Sciences, Columbia University, New York, New York*

^c *Cooperative Institute for Research in Environmental Sciences, University of Colorado Boulder, Boulder, Colorado*

^d *National Center for Atmospheric Research, Boulder, Colorado*

^e *NASA Goddard Institute for Space Studies, New York, New York*

(Manuscript received 26 October 2016, in final form 22 April 2017)

ABSTRACT

The tree-ring-based North American Drought Atlas (NADA), Monsoon Asia Drought Atlas (MADA), and Old World Drought Atlas (OWDA) collectively yield a near-hemispheric gridded reconstruction of hydroclimate variability over the last millennium. To test the robustness of the large-scale representation of hydroclimate variability across the drought atlases, the joint expression of seasonal climate variability and teleconnections in the NADA, MADA, and OWDA are compared against two global, observation-based PDSI products. Predominantly positive (negative) correlations are determined between seasonal precipitation (surface air temperature) and collocated tree-ring-based PDSI, with average Pearson's correlation coefficients increasing in magnitude from boreal winter to summer. For precipitation, these correlations tend to be stronger in the boreal winter and summer when calculated for the observed PDSI record, while remaining similar for temperature. Notwithstanding these differences, the drought atlases robustly express teleconnection patterns associated with El Niño–Southern Oscillation (ENSO), the North Atlantic Oscillation (NAO), the Pacific decadal oscillation (PDO), and the Atlantic multidecadal oscillation (AMO). These expressions exist in the drought atlas estimates of boreal summer PDSI despite the fact that these modes of climate variability are dominant in boreal winter, with the exception of the AMO. ENSO and NAO teleconnection patterns in the drought atlases are particularly consistent with their well-known dominant expressions in boreal winter and over the OWDA domain, respectively. Collectively, the findings herein confirm that the joint Northern Hemisphere drought atlases robustly reflect large-scale patterns of hydroclimate variability on seasonal to multidecadal time scales over the twentieth century and are likely to provide similarly robust estimates of hydroclimate variability prior to the existence of widespread instrumental data.

1. Introduction

Our ability to characterize hydroclimate variability from observations is confined to about 50–150 years of widespread instrumental records, limiting assessments of decadal–centennial variability and extreme events

that are not sufficiently sampled over a single century. The limitations of the instrumental record can be circumvented in part by analyzing proxy records that provide estimates of past hydroclimate variability over a range of time scales and resolutions (e.g., Jones et al. 2009; Masson-Delmotte et al. 2013). Tree-ring chronologies are an important proxy used in this context, as they provide annually resolved, seasonal estimates of hydroclimate conditions over the Common Era (CE; e.g., Cook et al. 2007, 2010b; Belmecheri et al. 2015; Routson et al. 2011; Woodhouse et al. 2010; Buckley et al. 2010).

Tree-ring-based gridded drought atlases that target the Palmer drought severity index (PDSI) are one important dendroclimatic product that has emerged over

Ⓞ Denotes content that is immediately available upon publication as open access.

Lamont-Doherty Earth Observatory Contribution Number 8128.

Corresponding author: Seung H. Baek, sb3210@columbia.edu

the last decade, comprising a vital source of information on CE hydroclimate (Cook et al. 2004, 2010a; E. Cook et al. 2015; Palmer et al. 2015; Stahle et al. 2016). Originally published in 2004, the North American Drought Atlas (NADA; Cook et al. 2004) is the most established of these efforts, with updates to incorporate additional tree-ring chronologies and increase resolution and spatial extent over North America (Cook et al. 2008, 2010b). The extensive spatial and temporal scope of the NADA allows for the study of North American hydroclimate conditions and the associated dynamics of hydroclimate variability over time scales that previously were not well sampled (e.g., Herweijer et al. 2007; Stahle et al. 2007; Cook et al. 2014a,b; Coats et al. 2016). These efforts have helped place modern drought conditions and dynamics in a paleoclimatic context, thus providing a longer-term perspective for evaluating the characteristics of modern drought and the roles that both natural variability and anthropogenic forcing play in contemporary hydroclimate and projected future conditions (e.g., Griffin and Anchukaitis 2014, Williams et al. 2015; Herweijer et al. 2007; Cook et al. 2014a; B. Cook et al. 2015). Additionally, the NADA has allowed for model-proxy comparisons over the last millennium (Smerdon et al. 2015, 2017; Coats et al. 2013b, 2015a,b,c; Stevenson et al. 2015, 2016) with implications for the interpretation of risk assessments from twenty-first-century model projections (Schmidt et al. 2014; Phipps et al. 2013; Ault et al. 2014, 2016; B. Cook et al. 2015).

Similar gridded hydroclimate reconstructions over other large areas of the Northern Hemisphere (NH) have been developed since the NADA, including the Monsoon Asia Drought Atlas (MADA; Cook et al. 2010a; Cook 2015) and the Old World Drought Atlas (OWDA; E. Cook et al. 2015). The MADA and OWDA have been used for important studies over their individual domains (e.g., Anchukaitis et al. 2010; Hernandez et al. 2015; Ummenhofer et al. 2013; Bell et al. 2011; Cook and Wolkovich 2016a; Cook et al. 2016) and additionally offer the prospect of using the NADA, OWDA, and MADA to collectively characterize widespread patterns of hydroclimate variability over a broad expanse of continental areas in the NH (Coats et al. 2016; Fang et al. 2014). Similarly, expansion of these efforts into the Southern Hemisphere (Palmer et al. 2015) will eventually provide the prospect of global analyses. Given the inherent seasonal expressions of precipitation and temperature teleconnections tied to large-scale dynamics and the seasonal representation of dendroclimatic records, this prospect necessitates a detailed evaluation of the seasonal and spatial sampling of the collective drought atlases.

St. George et al. (2010) first evaluated the seasonal influence of precipitation in the NADA and the associated seasonality and strength of El Niño–Southern Oscillation (ENSO) teleconnections during the interval 1900–78 CE (a period during which the NADA consists only of tree-ring records because it has not been spliced with any observation-based PDSI records). The authors demonstrated that while the NADA largely captures the precipitation influences and teleconnection patterns in the observational data, it does contain some seasonal biases; specifically, tree-ring-derived PDSI displays stronger winter precipitation signals and ENSO teleconnections over the U.S. Southwest and northern Mexico than are demonstrated in the instrumental data (St. George et al. 2010). These results have important implications for hydroclimate studies that use the NADA and indicate the need to conduct similar analyses of the MADA and OWDA. Furthermore, the impacts of large-scale atmosphere–ocean modes other than the ENSO such as the North Atlantic Oscillation (NAO; Fowler and Kilsby 2002; Burt and Howden 2013; Wedgbrow et al. 2002), Atlantic multidecadal oscillation (AMO; Kushnir et al. 2010; Ting et al. 2011; Enfield et al. 2001; Nigam et al. 2011; McCabe et al. 2004, 2008), and Pacific decadal oscillation (PDO; McCabe and Dettinger 2002; McCabe et al. 2004) highlight the importance of examining additional teleconnections associated with these ocean–atmosphere modes within the drought atlases.

With the above as motivation, we expand the analyses of St. George et al. (2010) to a joint evaluation of the NADA, MADA, and OWDA, each of which is based on independent tree-ring and observation-based PDSI data. We conduct analyses that are parallel to those of St. George et al. (2010) for the full NH and extend the evaluations in two important ways. First, in addition to the higher resolution and greater spatial extent of the joint drought atlases, we specifically evaluate the seasonal influence of temperature [St. George et al. (2010) only considered precipitation] in the tree-ring-based reconstructions of June–August (JJA) PDSI relative to PDSI based on observational estimates. Second, we evaluate the teleconnection patterns expressed across the three drought atlases for the NAO, PDO, and AMO, in addition to those of ENSO, the last of which was the only mode investigated by St. George et al. (2010). While these four modes do not account for all of the atmosphere–ocean modes that influence hydroclimate over the NH landmasses, they are some of the primary modes of influence and span a range of time scales from interannual to multidecadal. Taken collectively, our results are intended to guide future studies seeking to use the hemispheric collection of drought atlases for

TABLE 1. Descriptions of the three tree-ring datasets and key references.

Dataset	Resolution	Coverage	Total timespan (period analyzed in this study)	Calibration datasets	No. of chronologies	Primary reference for version used in this study	Example domain-specific references
LBDA NADA	0.5°	North America	0–2005 CE (1901–78 CE)	PDSI	1845	Cook et al. (2010b)	Coats et al. (2015a,b), Cook et al. (2007, 2014a,b), Herweijer et al. (2007), and St. George et al. (2010)
MADAv2	1.0°	Monsoon Asia	1250–2005 CE (1901–78 CE)	vdS PDSI	327	Cook et al. (2010a)	Anchukaitis et al. (2010) and Hernandez et al. (2015)
OWDA	0.5°	OWDA region	0–2012 CE (1901–78 CE)	vdS PDSI	106	E. Cook et al. (2015)	Cook and Wolkovich (2016) and Cook et al. (2016)

large-scale studies of hydroclimate variability and dynamics.

2. Data and methods

a. Observation and tree-ring-based PDSI data

PDSI is a normalized metric of soil moisture, with positive and negative values respectively reflecting wetter and drier conditions for a given region relative to a climatological baseline. PDSI is formulated on monthly precipitation and temperature data, accounting for both moisture supply and evapotranspiration, and has a persistence of about 12–18 months (e.g., Palmer 1965; Guttman 1998; Cook et al. 2007). We employ two observation-based PDSI datasets, one from van der Schrier et al. (2013) and the other from Dai (2011). The van der Schrier et al. (2013) PDSI (“vdS PDSI”) has 0.5° resolution from 1901 to 2012 and the Dai (2011) PDSI (“Dai PDSI”) has 2.5° resolution from 1850 to 2014. Both data products are monthly self-calibrating PDSI (Wells et al. 2004) using the Penman–Monteith (Penman 1948) formulation of potential evapotranspiration, and both have global land coverage. Monthly means of PDSI were used to derive JJA averages for the observation-based hydroclimate estimates (all PDSI values discussed in the remainder of this study are JJA averages). St. George et al. (2010) used instrumental PDSI developed from Cook et al. (2004), but we do not employ that dataset herein because it is limited to North America.

We use three gridded drought atlases that are further summarized in Table 1: the Living Blended Drought Atlas (LBDA) version of the NADA (Cook et al. 2010b), the MADA, version 2 (MADAv2; Cook et al. 2010a; Cook 2015), and the OWDA (E. Cook et al. 2015). The current versions of the NADA,

MADA, and OWDA have latitude–longitude grid resolutions of 0.5°, 1.0°, and 0.5°, respectively. All three atlases are reconstructed using a point-by-point regression method (PPR; Cook et al. 1996) and target JJA PDSI for reconstruction—the NADA is calibrated on PDSI (Heim et al. 2007) and the MADA and OWDA are calibrated on vdS PDSI. The PPR method uses, for each grid cell, tree-ring chronologies within a search radius of 450 km for the NADA (Cook et al. 2004) and 1000 km for the OWDA (E. Cook et al. 2015). Because of the irregular distribution of available tree-ring chronologies in the region called “monsoon Asia,” the MADA used multiple search radii (Cook et al. 2010a). The PPR method allows chronologies to be used in the reconstruction of more than one grid cell and only imposes local smoothing over the range of the search radius used in the calibration process (e.g., Cook et al. 1996). The method does not impose any large-scale pattern selections as a consequence of the underlying calibration scheme, as is common in other joint space–time reconstruction methods (e.g., Evans et al. 2002; Smerdon et al. 2011; Mann et al. 2009); large-scale patterns across each drought atlas are therefore emergent characteristics of the underlying data. The locally constrained characteristics of the PPR method also make each drought atlas entirely independent from the others, notwithstanding spatial autocorrelation features that arise due to covariance from the climate system. All PDSI products were subtracted then divided by their 1931–90 means and standard deviations, respectively, to recenter and normalize relative to a 1931–90 baseline. We constrain our analyses to the overlapping and independent period from 1901–78 for the tree-ring and observation-based PDSI datasets. While the 1901–78 period avoids splicing of tree-ring-derived and observation-based data, it does span the interval over

which the drought atlases have been calibrated on instrumental data (although this period also includes periods outside the calibration intervals).

b. Climate data and indices

The University of East Anglia Climatic Research Unit's (CRU) Time Series (TS), version 3.23, gridded dataset provides monthly precipitation and 2-m surface air temperature (SAT) data spanning 1901 to 2014 with 0.5° resolution (Harris et al. 2014). Following St. George et al. (2010), the December–February (DJF), March–May (MAM), and JJA periods are averaged over 1901–78 (1902–78 for DJF) to provide boreal winter, spring, and summer means, respectively. For precipitation, we also average from December to August to reflect the possibility of longer temporal integration of precipitation in the PDSI estimate of soil moisture.

The cold tongue index (CTI), defined as the average sea surface temperature (SST) anomaly over 6°N–6°S, 180°–90°W minus the mean global SST, is available from the University of Washington Joint Institute for the Study of the Atmosphere and Ocean (JISAO; online at http://research.jisao.washington.edu/data_sets/cti/). The CTI was used by St. George et al. (2010) as the ENSO index of choice and is employed herein for consistency. Again following St. George et al. (2010), the October to March months are taken from the CTI and averaged to produce 1901–78 means, reflecting the dominant season of ENSO impact.

Monthly NAO and PDO anomalies are available from the JISAO and span the intervals 1860–2009 and 1900–2016, respectively (online at http://research.jisao.washington.edu/data_sets/nao/ and http://research.jisao.washington.edu/data_sets/pdo/). The monthly AMO index is available from 1871 to the present from the NOAA/Earth System Research Laboratory (online at http://www.esrl.noaa.gov/psd/gcos_wgsp/Timeseries/AMO/). The December–March (DJFM), November–March, and JJA averages are used for the NAO, PDO, and AMO, respectively. Each of these averaging intervals represents the dominant season of impact of each mode of variability over large regions of the investigated domain, but we additionally consider other seasons in subsequent analyses.

c. Statistical methods

Point-to-point Pearson's correlation coefficients are calculated between PDSI (observation and tree-ring-based) and (i) precipitation and (ii) SAT over the NADA, MADA, and OWDA domains. Because the MADA has a coarser 1.0° resolution, precipitation and SAT are degraded to 1.0° resolution over the MADA domain using bilinear interpolation. The vdS PDSI has

been derived from the CRU TS precipitation and temperature data products. Thus, the reported correlations are representative of the PDSI transform of the data as opposed to differences between the CRU TS data and alternative PDSI input data. In contrast, the Dai PDSI uses a different CRU temperature dataset from Jones and Moberg (2003) and NCEP precipitation data (Dai et al. 2004). To avoid confounding the impact of the PDSI transform and different input datasets, we exclude precipitation and SAT correlations with the Dai PDSI.

Partial coefficients of determination r^2 are also calculated between PDSI (both observation and tree-ring-based) and (i) precipitation and (ii) SAT. The partial coefficients of determination quantify the PDSI variance explained by precipitation and SAT, respectively, while controlling for the covariance of the two variables (e.g., Warner 2013). These partial correlations are used to assess whether a specific variable dominates variance in the PDSI field by subtracting the partial r^2 values for SAT from those of precipitation. Positive and negative differences between the partial r^2 values indicate stronger influence of precipitation or SAT, respectively, while values close to zero point to either their equal contribution or collective absence of influence.

ENSO, NAO, PDO, and AMO teleconnection patterns are characterized using Pearson's correlation coefficients between each modal index and observation (both vdS and Dai PDSI) or tree-ring-based PDSI at each grid point. Following St. George et al. (2010), we also composite the drought atlases over years in which each respective modal index—CTI, NAO, AMO, and PDO—is one standard deviation above or below the 1901–78 mean. For the CTI, for instance, this yields El Niño and La Niña PDSI anomaly composites.

The similarity between spatial patterns in our analyses is characterized using the centered pattern correlation statistic (CPCS; Santer et al. 1995; Coats et al. 2013a) over the common grid points of two given datasets. All grid points are weighted by the square root of the cosine of their respective latitudes to account for decreasing surface area with increasing latitude prior to CPCS calculation. We calculate CPCS using Pearson's correlation coefficients, but do not assign p value significance because the spatial autocorrelation in the determined patterns ambiguously reduces the spatial degrees of freedom, and therefore the significance of the spatial correlations. For precipitation and temperature correlation plots, CPCS was calculated at 0.5° resolution. In all other cases, CPCS was calculated at 2.5° resolution, which was the lowest resolution of the data products used herein (Dai PDSI).

All point-to-point correlations and CPCS values were calculated using Pearson's correlation coefficients to

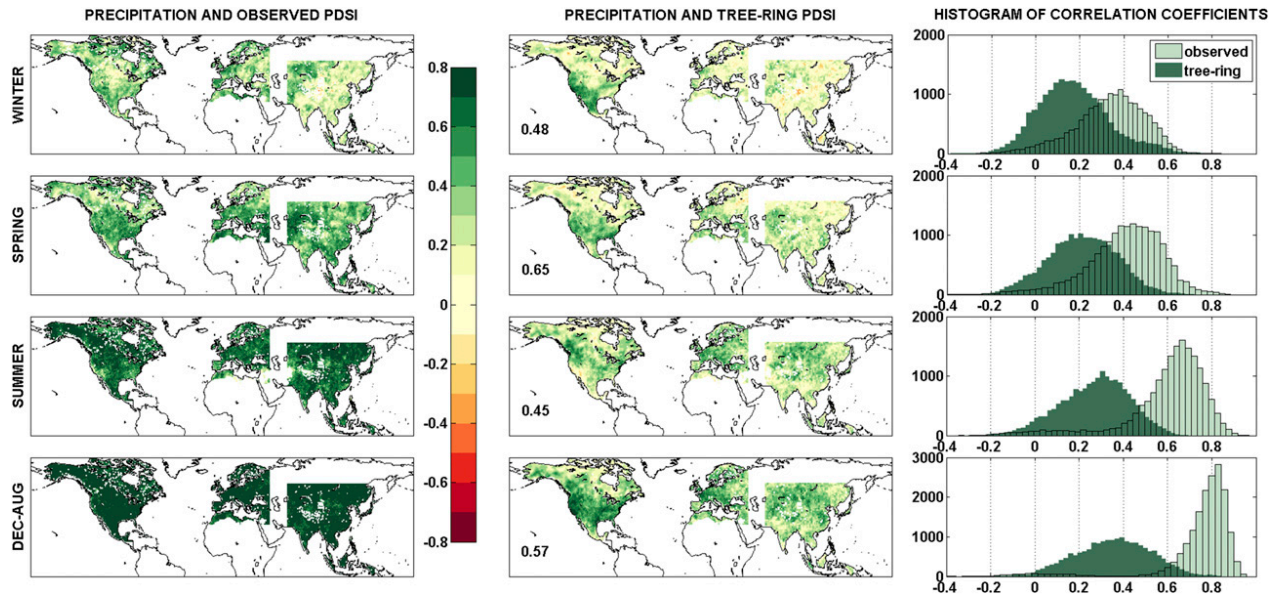


FIG. 1. (top)–(bottom) Pearson's point-to-point correlation coefficients between boreal winter (DJF), spring (MAM), summer (JJA), and 9-month (December–August) precipitation and (left) vdS and (center) tree-ring-based PDSI over the 1901/02–78 interval. Pearson's CPCS between the vdS and tree-ring-based PDSI correlation patterns are reported in the lower left of each tree-ring panel for the seasons in the associated row. (right) Correlation coefficients from each of the correlation maps are shown as histograms; coefficients associated with observed PDSI are binned at 1.0° resolution over the MADA domain in the histograms for consistency with the tree-ring product. A correlation value of 0.19 represents the one-tailed Student's t test at a 95% significance level ($p < 0.05$) for winter, spring, and summer.

reflect linear, parametric statistics. A Spearman's rank correlation was also used to test if our findings are robust when using a nonparametric test. The results using either correlation statistic were very similar and therefore are only shown for the Pearson's correlation statistic. All of the correlations in this study were also recalculated using detrended data; the patterns and correlations do not change in an appreciable manner after detrending.

3. Results

a. Seasonal influence of temperature and precipitation

Figure 1 shows maps and histograms of point-to-point Pearson's correlation coefficients calculated between seasonal and 9-month integrated precipitation and (i) vdS and (ii) tree-ring estimates of JJA PDSI. A correlation of 0.19 represents the one-tailed Student's t test at a 95% significance level ($p < 0.05$) for all histograms. The correlations of precipitation versus vdS PDSI are higher than precipitation versus tree-ring estimates of PDSI in part because instrumental precipitation data are used in calculating vdS PDSI. Correlation coefficients for the vdS PDSI become larger as the precipitation season progresses from boreal winter to summer (as can be seen in the histograms shifting positive), with JJA precipitation tending to have the greatest influence on JJA PDSI over all three domains (NADA, MADA, and OWDA). The correlation

coefficients also increase from boreal winter to summer over the majority of the NH landmass in the tree-ring-based PDSI, but do so more modestly. The 9-month integrated precipitation plots incorporate the precipitation signals of the three seasonal plots—in general, the 9-month plot is additive of the strongest signal from each of the three seasonal plots.

Figure 2 plots the maps and histograms of point-to-point Pearson's correlation coefficients calculated between seasonal SAT and (i) vdS and (ii) tree-ring estimates of JJA PDSI. A correlation value of 0.22 (0.23) represents the two-tailed Student's t test at a 95% significance level ($p < 0.05$) for spring and summer (winter) histograms. SAT has a widespread negative correlation with both PDSI estimates over most of the NH and the correlation coefficients increase in magnitude as the season progresses from boreal winter to summer across all three of the domains. The seasonal changes in correlation are evident in the histograms as well, which show the mean of the correlation coefficients shifting negative from boreal winter to summer.

The tree-ring-based PDSI correlation coefficient maps for precipitation and SAT overall resemble those for vdS PDSI. We quantify these similarities by calculating CPCS between the correlation maps estimated between precipitation and SAT and each seasonal field of tree-ring-based and vdS PDSI (i.e., between the left and middle columns in Figs. 1 and 2). Each season

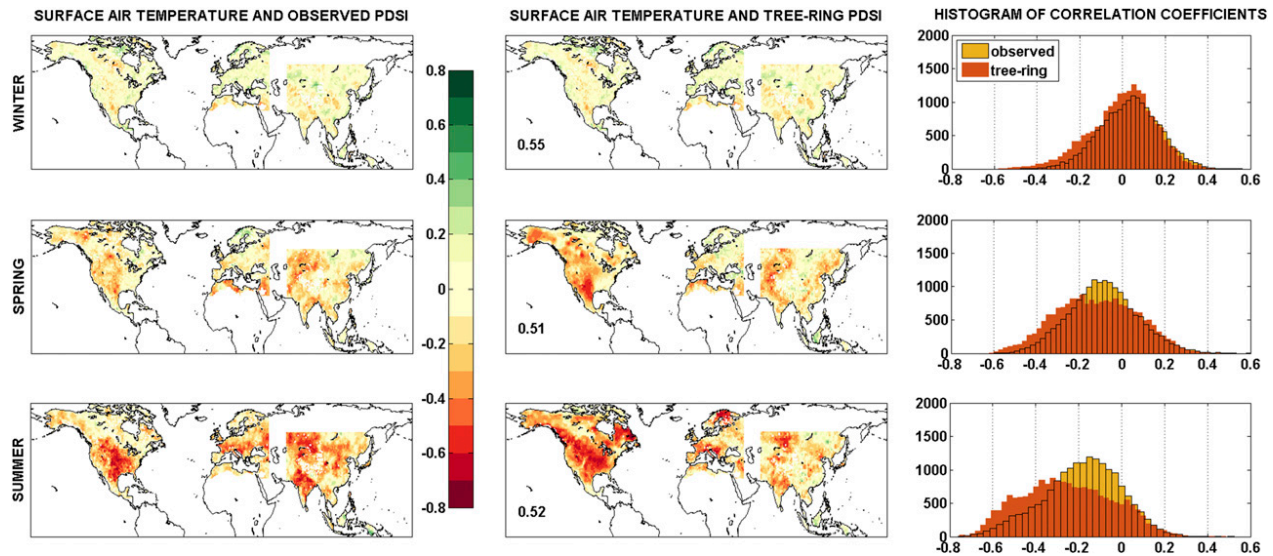


FIG. 2. As in Fig. 1, but for surface air temperature. A correlation value of 0.22 (0.23) represents the two-tailed Student's t test at a 95% significance level ($p < 0.05$) for spring and summer (winter).

yields a CPCS between the observation and tree-ring-based PDSI in the range of 0.45–0.65. CPCS is highest in the boreal spring and winter for precipitation and SAT, respectively. One important caveat regarding the comparison of the precipitation and temperature correlations is that vdS PDSI is derived from CRU TS precipitation and temperature data. This guarantees strong correlations between the CRU TS forcing data and the vdS PDSI, regardless of whether they are accurate estimates of historical conditions. While differences between the precipitation correlation patterns with tree-ring-based and vdS PDSI may reflect differences in the manner in which the tree rings integrate precipitation relative to the observational estimate, such differences may also reflect biases in the instrumental data. For instance, data coverage over much of the monsoon Asia domain, in particular the East Asian monsoon regions, is poor prior to about 1950 (Cook et al. 2010a). In contrast, the vdS PDSI is guaranteed to correlate well with the CRU TS precipitation because it is derived from it.

Figure 3 shows the difference between the partial r^2 values calculated using precipitation and SAT and the vdS and tree-ring-based PDSI. The precipitation coefficients are predominantly larger than the SAT coefficients in the vdS PDSI fields across all three seasons. Correlation between precipitation and the tree-ring PDSI field is weaker, particularly over the summer NADA domain where temperature coefficients are predominantly greater than the precipitation counterparts. Overall, precipitation dominates the PDSI field to a greater extent in vdS PDSI than tree-ring-based

PDSI, but again the caveat regarding the use of CRU TS precipitation and temperature in the vdS PDSI calculation is applicable.

b. ENSO teleconnections

The teleconnection patterns associated with ENSO, as measured by the CTI during the preceding winter, for the vdS, Dai, and tree-ring-based PDSI are shown in Fig. 4. Both the strength and pattern of the ENSO teleconnection with PDSI are broadly comparable between the observation and tree-ring-based estimates, indicating that ENSO teleconnections are robustly captured in the dendroclimatic data. In North America, for instance, a strong El Niño dipole with a wet area over the southwestern United States and northern Mexico and a dry area over the northwestern United States and western Canada is prominent across the vdS, Dai, and tree-ring-based PDSI products. There is also an ENSO dipole over monsoon Asia, with positive PDSI over much of the northwest and southeast parts of the domain associated with El Niño and La Niña events, respectively.

The coherence in the strength and pattern of ENSO teleconnections across the NH is reflected in the high CPCS value of 0.70 (0.59) between the tree-ring-based and vdS (Dai) PDSI patterns. Note, however, that while the ENSO patterns are largely consistent across all three PDSI products, the vdS PDSI teleconnection maps are less spatially coherent than their Dai or tree-ring PDSI counterparts in Fig. 4 or the ENSO results presented in St. George et al. (2010). PDSI formulation is unlikely to be the primary cause of the discrepancy, as both the vdS

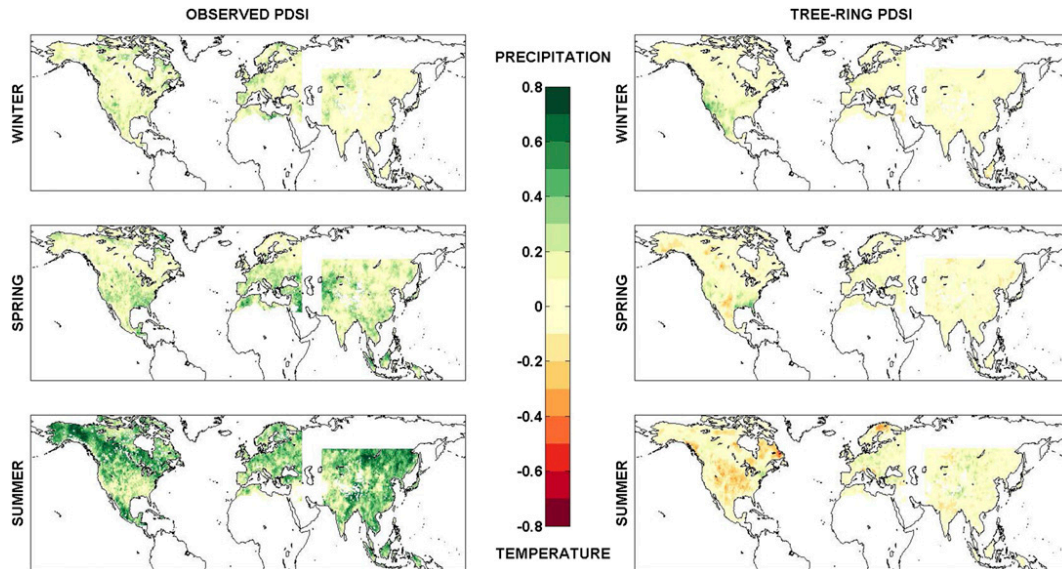


FIG. 3. Difference between the squared partial correlations between PDSI and (i) precipitation and (ii) temperature (top)–(bottom) for boreal winter (DJF), spring (MAM), and summer (JJA) for (left) vdS and (right) tree-ring-based PDSI over the 1901/02–78 interval. Positive and negative partial r^2 values indicate that either precipitation or SAT respectively dominate the explained variance in PDSI. Values close to zero point to either their equal contribution or a collective absence of their influence.

PDSI and the Dai PDSI use the self-calibrating Penman–Monteith method. Rather, the discrepancy may be due to the fact that the vdS PDSI product considers the spatially heterogeneous effects of snow cover and vegetation (van der Schrier et al. 2013), which may

explain the greater spatial heterogeneity of the results for the vdS PDSI across all of our analyses. Finally, the tree-ring-based composites of El Niño and La Niña events ($N = 14$ and 10 yr, respectively) compare more weakly with the observational data, likely due to the

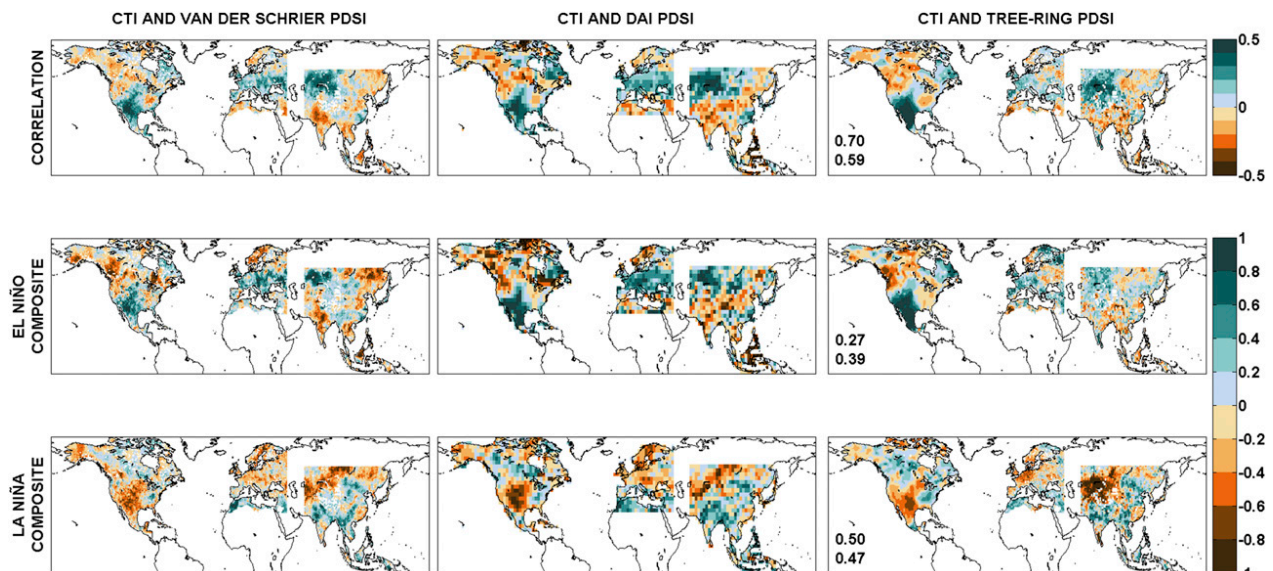


FIG. 4. (top) Pearson's correlation coefficients between the CTI (October–March) and (left) vdS, (center) Dai, and (right) tree-ring-based PDSI. A correlation value of 0.22 represents the two-tailed Student's t test at a 95% significance level ($p < 0.05$). Also shown are PDSI anomaly composites for years in which the CTI was one standard deviation (middle) above (El Niño) and (bottom) below (La Niña) the 1901–78 mean, with 14 and 10 events, respectively. Pearson's CPCS is reported (right) for each associated row between (i) tree-ring-based and vdS PDSI patterns (top number at bottom left of the panels) and (ii) tree-ring-based and Dai PDSI patterns (bottom number at the bottom left of the panels).

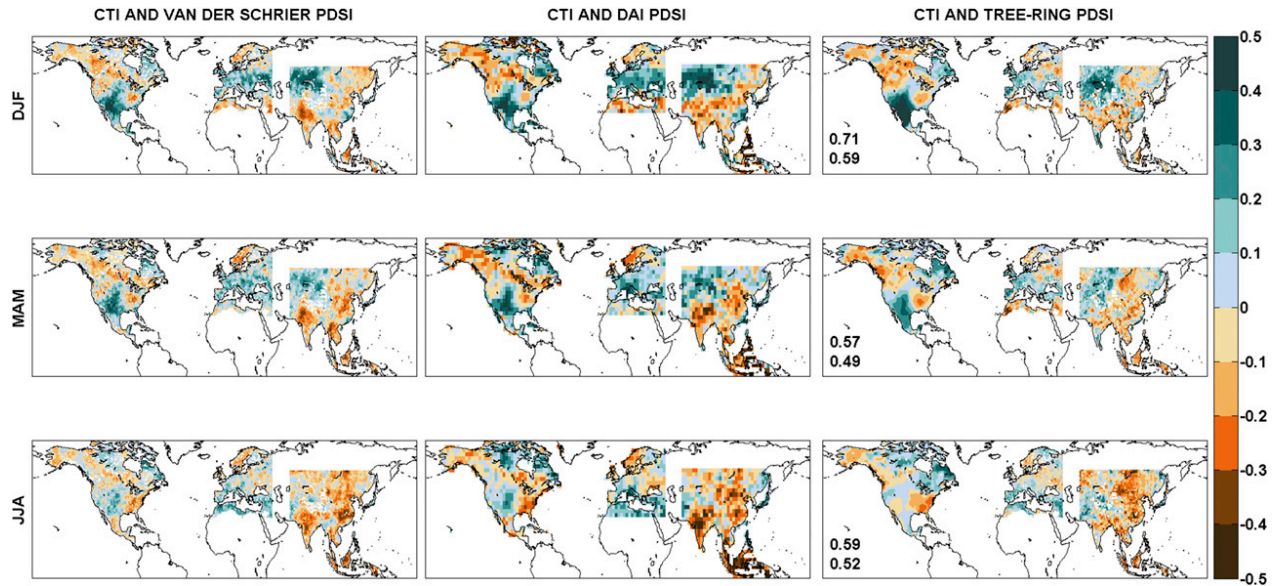


FIG. 5. Pearson's correlation coefficients between the CTI (October–March) and (left) vdS, (center) Dai, and (right) tree-ring-based (right) PDSI by season. A correlation value of 0.22 (0.23) represents the two-tailed Student's t test at a 95% significance level ($p < 0.05$) in boreal spring and summer (winter). (top) DJF, (middle) MAM, and (bottom) JJA represent winter, spring, and summer, respectively. Pearson's CPCS is reported (right) for each season between (i) tree-ring-based and vdS PDSI patterns (top number at bottom left of the panels) and (ii) tree-ring-based and Dai PDSI patterns (bottom number at bottom left of the panels).

smaller sample sizes associated with the composites. Nevertheless, the tree-ring-based composites are very similar to the CTI correlation patterns across the two observational PDSI products.

When broken down into seasons, the ENSO teleconnection patterns (Fig. 5) indicate that boreal winter is the dominant season of hydroclimatic impact on JJA PDSI, not only over North America but also over the entire domain spanned by the three drought atlases. In general, the teleconnection pattern diminishes from boreal winter into spring and during the coincident summer. This is consistent with the typical seasonal evolution of ENSO anomalies that grow through the boreal summer and fall, peak in the winter, and subsequently diminish into the following spring and summer (Sarachik and Cane 2010). The southern and eastern regions of the MADA domain are exceptions to the weakening ENSO teleconnection signals from winter to summer; dry conditions in summer are enhanced relative to the spring and comparable to those over the winter, which is consistent with the known impact of ENSO on the South Asian peak monsoon season through its modulation of the Walker circulation (Sarachik and Cane 2010). However, an anomalous western Pacific anticyclone in the decaying-year summer has been shown to be associated with positive precipitation anomalies over some of the East Asian monsoon regions (Wu et al. 2009).

c. NAO teleconnections

Teleconnection patterns for the DJFM NAO show a strong wet–dry dipole over northern and southern Europe across all three PDSI products (Fig. 6), demonstrating that tree-ring-based PDSI robustly captures NAO influences over the European domain. The NAO teleconnection pattern is further expressed by drying over India and East Asia, where the winter NAO may have an inverse relationship with the Indian and East Asian summer monsoon precipitation, respectively (Dugam et al. 1997; Sung et al. 2006). There is also a strong positive correlation between the NAO and observed and tree-ring-based PDSI in the central and eastern United States (Fye et al. 2006).

Similar to the results for ENSO, the tree-ring-based drought atlases capture the patterns in the observational PDSI products, as is reflected by the CPCS value between the NAO teleconnection maps for the tree-ring-based PDSI and (i) vdS PDSI (CPCS = 0.60) and (ii) Dai PDSI (CPCS = 0.54). It should be noted that while CPCS values in both the positive and negative composites of NAO decrease relative to those in the correlation-based teleconnection map, the pattern correlation in the positive composite deteriorates substantially more (vdS PDSI CPCS = 0.02 and Dai PDSI CPCS = 0.14). Some of this may be attributable to the very wet conditions over central-western North

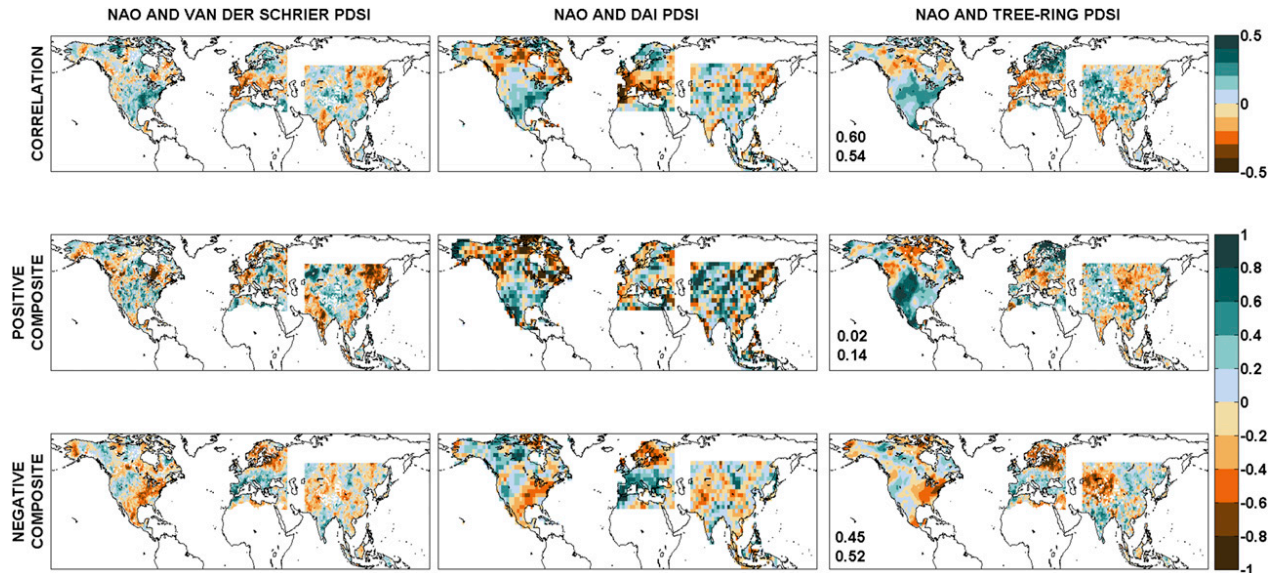


FIG. 6. (top) Pearson's point-to-point correlation coefficients between the NAO index (DJFM) and (left) vdS, (center) Dai, and (right) tree-ring-based PDSI. A correlation value of 0.22 represents the two-tailed Student's t test at a 95% significance level ($p < 0.05$). Also shown are PDSI anomaly composites for years in which the NAO was one standard deviation (middle) above and (bottom) below the 1901–78 mean, with 10 and 13 events, respectively. The CPCS for the teleconnection patterns is calculated with the same convention as reported for Fig. 4 and shown in (right).

America in the tree-ring-based PDSI, which are not strongly featured in the vdS PDSI or Dai PDSI counterparts.

Despite the relatively small correlations between JJA PDSI and precipitation and temperature in the boreal winter and spring (Figs. 1 and 2), the spatiotemporal variability of JJA PDSI contains a clear DJFM NAO signal over the European domain (Fig. 6). To further demonstrate the NAO influence across Europe, we decompose the OWDA into empirical orthogonal functions (EOFs) over the 1901–78 period using an area-weighted field. The first EOF is shown in Fig. 7, accounting for 20% of the variability in the OWDA, and reveals a spatial pattern that is very similar to the correlation pattern between the DJFM NAO index and OWDA PDSI (the two patterns have a CPCS value of 0.84). The NAO index and the first principal component (PC) from the EOF decomposition of the OWDA field also are significantly correlated ($r = 0.43$, $p < 0.01$). These results indicate that despite the variable seasonal influences of temperature and precipitation on PDSI over Europe, the dominant winter influence of the NAO is robustly captured in the OWDA.

d. PDO teleconnections

PDO teleconnection patterns are consistent across all three PDSI products, as represented in Fig. 8. These patterns are similar to those expressed in the ENSO teleconnection patterns (Fig. 4). For example, positive

correlations exist over Mexico and the U.S. Southwest and over much of Europe, while a positive–negative dipole is evident over northwestern and southeastern Asia. For most regions in the three drought atlases, the positive- and negative-phase composites are roughly mirror images and consistent with the patterns implied by the correlation-based teleconnection map. One

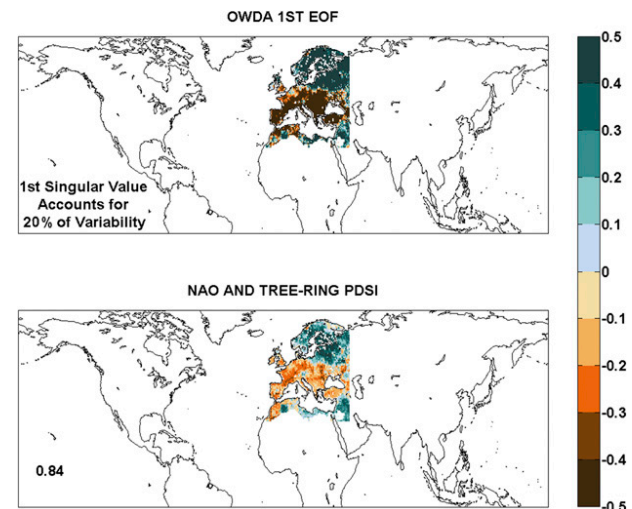


FIG. 7. A comparison of (top) the first EOF pattern in the OWDA and (bottom) Pearson's correlation coefficients between the NAO index (DJFM) and tree-ring-based PDSI over the OWDA domain. CPCS calculated between the represented patterns are shown for Pearson's coefficients.

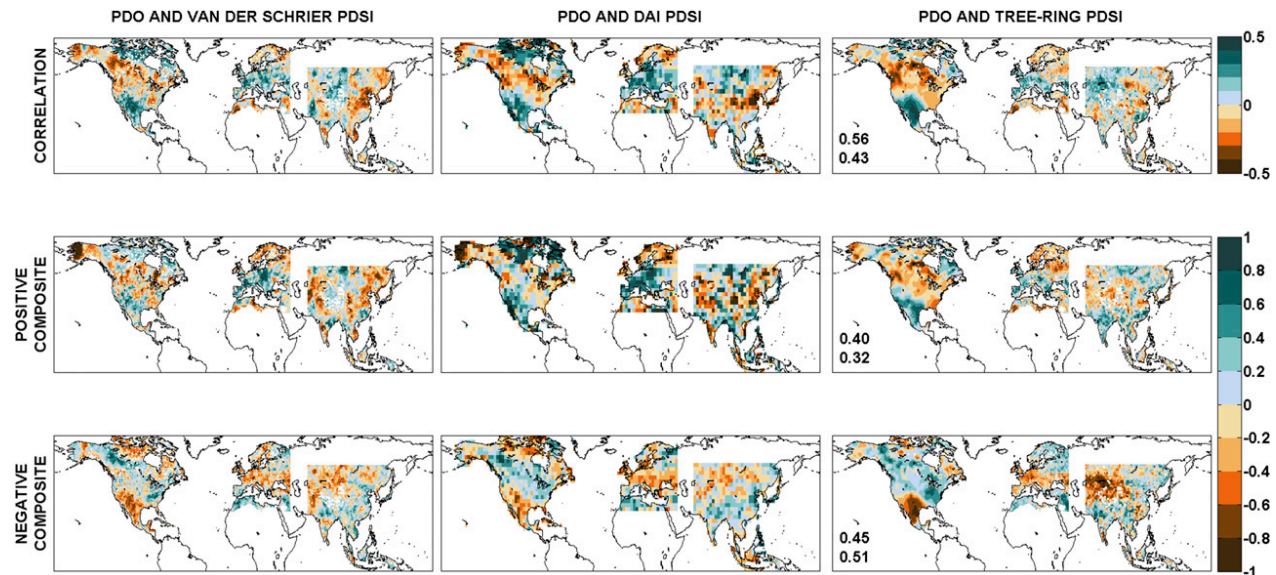


FIG. 8. (top) Pearson's point-to-point correlation coefficients between the PDO index (November–March) and (left) vdS, (center) Dai, and (right) tree-ring-based PDSI. A correlation value of 0.22 represents the two-tailed Student's t test at a 95% significance level ($p < 0.05$). PDSI anomaly composites are shown for years in which the PDO was one standard deviation (middle) above and (bottom) below the 1901–78 mean, with 16 and 15 events, respectively. The CPCS for the teleconnection patterns is calculated with the same convention as reported for Fig. 4 and shown in (right).

exception is over the northwest region of the MADA, which shows drying for both the positive and negative phase composites.

e. AMO teleconnections

The AMO teleconnection maps are plotted in Fig. 9. These patterns and correlations are expected to be the

least robust of our analysis, given the multidecadal time scale of the AMO and the comparatively short time scale over which our evaluation is performed. CPCS values between the tree-ring-based PDSI and (i) vdS and (ii) Dai PDSI are 0.45 and 0.33, respectively. Although the AMO teleconnection maps demonstrate lower CPCS values than those of the other modal

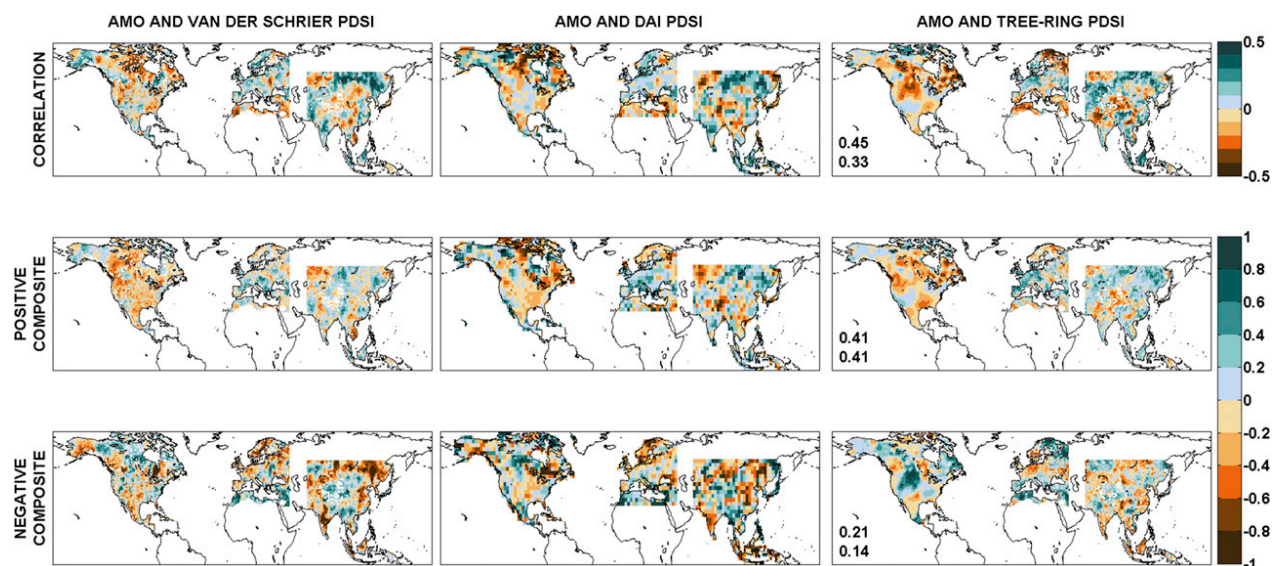


FIG. 9. (top) Pearson's correlation coefficients between the AMO index (JJA) and (left) vdS, (center) Dai, and (right) tree-ring-based PDSI. A correlation value of 0.22 represents the two-tailed Student's t test at a 95% significance level ($p < 0.05$). PDSI anomaly composites are for years in which the AMO was one standard deviation (middle) above and (bottom) below the 1901–78 mean, with 15 and 17 events, respectively. The CPCS for the teleconnection patterns is calculated with the same convention as reported for Fig. 4 and shown in (right).

indices, they are nonetheless broadly consistent across all three PDSI products. Much like the CTI and PDO figures, the pattern observed in the correlation-based AMO teleconnection map for the tree-ring-based PDSI is also largely reproduced in the positive phase composites. An exception is that while the pattern in the negative phase composite is inverted relative to the positive phase composite for the tree-ring-based PDSI, this is less true for the vdS and Dai PDSI composites. This is particularly the case over the NADA domain where the dry pattern seen in the positive composites remains, although less severely, in the negative composites.

4. Discussion

The seasonal influences of precipitation and temperature in the NH drought atlases are similar to the patterns captured in the observation-based PDSI. The increasingly positive (negative) correlation between boreal (i) winter, (ii) spring, and (iii) summer precipitation (temperature) and observation-based JJA PDSI is intuitive because, despite the persistence built into the PDSI calculation, JJA PDSI is still most influenced by JJA conditions. For temperature, the strengthening of the negative correlation from boreal winter through summer is further expected as higher temperatures are associated with larger evaporative demand (and generally coupled to reduced precipitation; e.g., Livneh and Hoerling 2016; Yin et al. 2014). Over North America, this is consistent with Williams et al. (2013), who showed temperature to account for more variability in tree-ring records of the U.S. Southwest than would be expected if the only effect of warm temperature on trees was through a decrease in soil moisture.

The contrast in how precipitation and temperature are expressed in the observation and tree-ring-based PDSI is attributable, at least in part, to the fact that tree-ring growth reflects more than current growing-season soil moisture (e.g., Anderegg et al. 2015). While the PDSI formulation itself imposes a lag relationship with precipitation and temperature (Karl 1986; Mishra and Singh 2010), interactions between tree physiology and environment such as seasonal carbohydrate storage (Barbaroux and Bréda 2002) may impose an even longer lag in growth responses. Nevertheless, the tree-ring PDSI reconstruction method does incorporate autoregressive prewhitening to account for both physiological and climatological persistence differences between instrumental PDSI and tree rings (Cook et al. 1999). In winter-dominated precipitation regions, contrasts in seasonality may also be attributed to the role of

snowmelt in delayed moisture delivery during the spring, particularly in high-elevation regions where snow accumulation can be significant (St. George et al. 2010). Such moisture delivery may contribute to the enhanced winter precipitation signal in the U.S. Southwest in tree-ring-based PDSI. It may also be why correlations between U.S. Southwest tree-ring-based PDSI and ENSO tend to be stronger than the vdS or Dai PDSI counterparts, as vdS PDSI only parameterizes snow cover using a simple positive-degree-day model with surface temperature and accumulated precipitation inputs (van der Schrier et al. 2013) and Dai PDSI does not account for snow accumulation. These considerations may help explain some of the differences in expressions of seasonal precipitation and temperature between JJA PDSI estimates from observations and dendroclimatic records. As noted previously, it is also likely that our comparison favors the relationships between precipitation and temperature in the vdS PDSI because the CRU TS data were used to derive the PDSI estimates. Inaccuracies in the instrumental data will diminish the correlations between tree-ring PDSI and precipitation and temperature, while the same correlations computed for vdS PDSI will remain strong.

Despite the noted differences between the impacts of precipitation and temperature on the observation and tree-ring-based PDSI fields, it is remarkable that the large-scale teleconnection patterns characterized by the different PDSI products are broadly comparable. This is first evident in the CTI teleconnection patterns that are consistent with the findings of St. George et al. (2010) over North America, while further reflecting the canonical understanding of ENSO impacts across the NH. For example, dry and wet conditions over the respective northwestern and southern U.S. regions are associated with a positive ENSO phase (e.g., Piechota and Dracup 1996), and our results are also consistent with the well-known connection between droughts over India and El Niño events (e.g., Krishna Kumar et al. 2006). Furthermore, the seasonal patterns of ENSO in Fig. 5 display ENSO correlations that are strongest during DJF not only over North America but also over the whole of the NH, consistent with the dominant expression of ENSO during boreal winter. While the ENSO imprint diminishes over the NADA and OWDA domains from boreal winter to spring and summer, the teleconnections between PDSI and ENSO persist into the summer in the southern and eastern domains of the MADA due to the strong association between El Niño and a weak South Asian summer monsoon (Varikoden et al. 2015). The consequence is a drying over the region (Varikoden et al. 2015) caused by the interaction of the South Asian monsoon with summer ENSO and subsequent

atmospheric circulation changes (Wu et al. 2012). The fact that these seasonal dependencies are represented in the drought atlases is an important demonstration that tree-ring-based PDSI, despite its JJA representation, is spatially sensitive to seasonal dynamics.

The NAO is the dominant mode of climate variability over the North Atlantic region, with extensive climate impacts on European storm trajectories, temperature, and precipitation (Trigo et al. 2002; Mares et al. 2002), and is therefore expected to have strong teleconnection influences over the OWDA domain. This was demonstrated in Fig. 6, where a dipole exists over the OWDA region in the teleconnection patterns, and in the domain-specific EOF analysis represented in Fig. 7. The strong spatial coherence between the leading EOF and winter NAO teleconnection pattern, as well as the positive and significant correlation between the winter NAO index and the leading OWDA PC, demonstrates that the boreal winter NAO remains strongly expressed in the JJA PDSI EOF pattern. This suggests not only that the tree-ring-based PDSI robustly captures the influences of the NAO, but also that the OWDA may be suitable for reconstructing the NAO index prior to the instrumental record.

The PDO is a consequence of ENSO, ocean memory, and Kuroshio–Oyashio system changes (Newman et al. 2003, 2016). The PDO teleconnection map produces a pattern very similar to that associated with the CTI, confirming the strong link between the PDO and ENSO. For instance, the strong ENSO dipole over central and northern Mexico (positive during El Niño) and northwestern United States and Canada (positive during La Niña) is largely present in the PDO teleconnection pattern (Fig. 8). The same is true for the dipole over the northwest and southeast domains of monsoon Asia associated with El Niño and La Niña events, respectively. We also note that significant negative correlations in northern China are consistent with previous results (Qian and Zhou 2014). While the PDO composites do retain patterns similar to the ENSO teleconnection pattern, they are weakened in many locations. This weakening may be due in part to the lower frequencies inherent in the PDO, and therefore may include less extreme PDO events during the 1901–78 analysis interval.

The AMO exhibits the longest periods of variability of the four modal indices analyzed (e.g., Ting et al. 2011). Figure 9 shows that tree-ring-based PDSI still produces AMO teleconnection patterns broadly consistent with observation-based PDSI. Furthermore, the drying associated with a positive AMO is consistent with several previous studies. Kushnir et al. (2010) showed that warm tropical North Atlantic SSTs lead to decreased

precipitation over the United States and northern Mexico; McCabe et al. (2004) associated positive phases of the AMO with drying over the conterminous United States. The drying in Mexico and the central plains of the United States, as represented in Fig. 9, is consistent with these reported AMO teleconnections. The spatial correlations between the teleconnection patterns represented by the tree-ring and observation-based PDSI, however, are diminished relative to the other higher-frequency modes when measured by the CPCS values. The composites also demonstrate lower pattern similarities that are likely due to the fact that 1901–78 is too short an interval to robustly capture the multidecadal frequencies of the AMO. As a consequence, the results of our AMO analysis are the most ambiguous, a result that is consistent with pseudoproxy experiments and attempts to reconstruct the AMO from the NH drought atlases (Coats et al. 2016).

5. Conclusions

Our analyses of the hemispheric collection of drought atlases parallel the efforts of St. George et al. (2010), who focused on the NADA domain and its association with the CTI, while extending our analysis to evaluate temperature impacts and assess teleconnection patterns associated with three additional modes: the NAO, PDO, and AMO. Where our analyses overlap, our results strongly corroborate those of St. George et al. (2010). Our analysis of the full NH additionally demonstrates that the three drought atlases are skillful at capturing the large-scale signatures of the NAO, PDO, and AMO on interannual, decadal, and multidecadal time scales. These findings are important in the context of future work seeking to use the collective NH drought atlases to characterize aspects of past hemispheric or continental-scale hydroclimate variability.

When complemented with additional atmospheric and ocean surface data the now hemispheric collection of drought atlases can provide powerful insights into the causes and dynamics of rare, low-frequency and/or extremely widespread events. Examples of such events include multidecadal (e.g., Coats et al. 2013b, 2015b, 2016; Stevenson et al. 2015; Seager et al. 2008) or pancontinental (e.g., Cook et al. 2014b; Coats et al. 2015a) droughts, both of which are poorly sampled in the instrumental record and require a broad spatial sampling for investigation. This potential application is particularly promising in light of expansion efforts of the drought atlases into the Southern Hemisphere (Palmer et al. 2015). A global collection of drought atlases will ultimately provide a cohesive record of global hydroclimate variability over the last thousand years or more,

and therefore expand our understanding of how hydroclimate has varied broadly in space over decades and centuries. The present study is therefore an important first step toward understanding the joint spatiotemporal signals in the growing collection of drought atlases and how they can be used to investigate and reconstruct hemispheric and global hydroclimate dynamics.

Acknowledgments. This work was supported in part by NSF Grants AGS-1243204 and AGS-1401400. B. I. Cook is supported by the NASA Modeling, Analysis, and Prediction program.

REFERENCES

- Anchukaitis, K. J., B. M. Buckley, E. R. Cook, B. I. Cook, R. D. D'Arrigo, and C. M. Ammann, 2010: Influence of volcanic eruptions on the climate of the Asian monsoon region. *Geophys. Res. Lett.*, **37**, L22703, doi:10.1029/2010GL044843.
- Anderegg, W. R. L., and Coauthors, 2015: Pervasive drought legacies in forest ecosystems and their implications for carbon cycle models. *Science*, **349**, 528–532, doi:10.1126/science.aab1833.
- Ault, T. R., J. E. Cole, J. T. Overpeck, G. T. Pederson, and D. M. Meko, 2014: Assessing the risk of persistent drought using climate model simulations and paleoclimate data. *J. Climate*, **27**, 7529–7549, doi:10.1175/JCLI-D-12-00282.1.
- , J. S. Mankin, B. I. Cook, and J. E. Smerdon, 2016: Relative impacts of mitigation, temperature, and precipitation on 21st-century megadrought risk in the American Southwest. *Sci. Adv.*, **2**, e1600873, doi:10.1126/sciadv.1600873.
- Barbaroux, C., and N. Bréda, 2002: Contrasting distribution and seasonal dynamics of carbohydrate reserves in stem wood of adult ring-porous sessile oak and diffuse-porous beech trees. *Tree Physiol.*, **22**, 1201–1210, doi:10.1093/treephys/22.17.1201.
- Bell, A. R., B. I. Cook, K. J. Anchukaitis, B. M. Buckley, and E. R. Cook, 2011: Repurposing climate reconstructions for drought prediction in Southeast Asia. *Climatic Change*, **106**, 691–698, doi:10.1007/s10584-011-0064-2.
- Belmecheri, S., F. Babst, E. R. Wahl, D. W. Stahle, and V. Trouet, 2015: Multi-century evaluation of Sierra Nevada snowpack. *Nat. Climate Change*, **6**, 2–3, doi:10.1038/nclimate2809.
- Buckley, B. M., and Coauthors, 2010: Climate as a contributing factor in the demise of Angkor, Cambodia. *Proc. Natl. Acad. Sci. USA*, **107**, 6748–6752, doi:10.1073/pnas.0910827107.
- Burt, T. P., and N. J. K. Howden, 2013: North Atlantic Oscillation amplifies orographic precipitation and river flow in upland Britain. *Water Resour. Res.*, **49**, 3504–3515, doi:10.1002/wrcr.20297.
- Coats, S., J. E. Smerdon, B. I. Cook, and R. Seager, 2013a: Stationarity of the tropical Pacific teleconnection to North America in CMIP5/PMIP3 model simulations. *Geophys. Res. Lett.*, **40**, 4927–4932, doi:10.1002/grl.50938.
- , —, R. Seager, B. I. Cook, and J. F. González-Rouco, 2013b: Megadroughts in southwestern North America in ECHO-G millennial simulations and their comparison to proxy drought reconstructions. *J. Climate*, **26**, 7635–7649, doi:10.1175/JCLI-D-12-00603.1.
- , B. I. Cook, J. E. Smerdon, and R. Seager, 2015a: North American pancontinental droughts in model simulations of the last millennium. *J. Climate*, **28**, 2025–2043, doi:10.1175/JCLI-D-14-00634.1.
- , J. E. Smerdon, B. I. Cook, and R. Seager, 2015b: Are simulated megadroughts in the North American Southwest forced? *J. Climate*, **28**, 124–142, doi:10.1175/JCLI-D-14-00071.1.
- , —, R. Seager, D. Griffin, and B. I. Cook, 2015c: Winter-to-summer precipitation phasing in southwestern North America: A multicentury perspective from paleoclimatic model–data comparisons. *J. Geophys. Res. Atmos.*, **120**, 8052–8064, xxx.
- , —, B. I. Cook, R. Seager, E. R. Cook, and K. J. Anchukaitis, 2016: Internal ocean–atmosphere variability drives megadroughts in western North America. *Geophys. Res. Lett.*, **43**, 9886–9894, doi:10.1002/2016GL070105.
- Cook, B. I., and E. M. Wolkovich, 2016: Climate change decouples drought from early winegrape harvests in France. *Nat. Climate Change*, **6**, 715–719, doi:10.1038/nclimate2960.
- , R. Seager, and J. E. Smerdon, 2014a: The worst North American drought year of the last millennium: 1934. *Geophys. Res. Lett.*, **41**, 7298–7305, doi:10.1002/2014GL061661.
- , J. E. Smerdon, R. Seager, and E. R. Cook, 2014b: Pancontinental droughts in North America over the last millennium. *J. Climate*, **27**, 383–397, doi:10.1175/JCLI-D-13-00100.1.
- , T. R. Ault, and J. E. Smerdon, 2015: Unprecedented 21st century drought risk in the American Southwest and Central Plains. *Sci. Adv.*, **1**, e1400082, doi:10.1126/sciadv.1400082.
- , K. J. Anchukaitis, R. Touchan, D. M. Meko, and E. R. Cook, 2016: Spatiotemporal drought variability in the Mediterranean over the last 900 years. *J. Geophys. Res. Atmos.*, **121**, 2060–2074, doi:10.1002/2015JD023929.
- Cook, E. R., 2015: Asian monsoon variability over the past millennium reconstructed from long tree-ring records: The Monsoon Asia Drought Atlas, version 2 (MADAv2). AGU Chapman Conference: “Evolution of the Asian Monsoon and its Impact on Landscape, Environment and Society: Using the Past as the Key to the Future,” Hong Kong, China, Amer. Geophys. Union. [Abstract available online at <https://agu.confex.com/agu/monsoon/webprogram/Paper37251.html>.]
- , D. M. Meko, D. W. Stahle, and M. K. Cleaveland, 1996: Tree-ring reconstructions of past drought across the conterminous United States: Tests of a regression method and calibration/verification results. *Tree Rings, Environment, and Humanity: Proceedings of the International Conference on Radiocarbon*. J. S. Dean, D. M. Meko, and T. W. Swetnam, Eds., University of Arizona Press, 155–169.
- , —, —, and —, 1999: Drought reconstructions for the continental United States. *J. Climate*, **12**, 1145–1162, doi:10.1175/1520-0442(1999)012<1145:DRFTCU>2.0.CO;2.
- , C. A. Woodhouse, C. M. Eakin, D. M. Meko, and D. W. Stahle, 2004: Long-term aridity changes in the western United States. *Science*, **306**, 1015–1018, doi:10.1126/science.1102586.
- , R. Seager, M. A. Cane, and D. W. Stahle, 2007: North American drought: Reconstructions, causes, and consequences. *Earth-Sci. Rev.*, **81**, 93–134, doi:10.1016/j.earscirev.2006.12.002.
- , and Coauthors, 2008: North American summer PDSI reconstructions, version 2a. IGBP PAGES/World Data Center for Paleoclimatology, Data Contribution Series 2008-046. [Available online at <ftp://ftp.ncdc.noaa.gov/pub/data/paleo/drought/NAmericanDroughtAtlas.v2/>.]
- , K. J. Anchukaitis, B. M. Buckley, R. D. D'Arrigo, G. C. Jacoby, and W. E. Wright, 2010a: Asian monsoon failure and megadrought during the last millennium. *Science*, **328**, 486–489, doi:10.1126/science.1185188.
- , R. Seager, R. R. Heim Jr., R. S. Vose, C. Herweijer, and C. Woodhouse, 2010b: Megadroughts in North America:

- Placing IPCC projections of hydroclimatic change in a long-term palaeoclimate context. *J. Quat. Sci.*, **25**, 48–61, doi:10.1002/jqs.1303.
- , and Coauthors, 2015: Old World megadroughts and pluvials during the Common Era. *Sci. Adv.*, **1**, e1500561, doi:10.1126/sciadv.1500561.
- Dai, A., 2011: Characteristics and trends in various forms of the Palmer drought severity index during 1900–2008. *J. Geophys. Res.*, **116**, D12115, doi:10.1029/2010JD015541.
- , K. E. Trenberth, and T. Qian, 2004: A global dataset of Palmer drought severity index for 1870–2002: Relationship with soil moisture and effects of surface warming. *J. Hydrometeorol.*, **5**, 1117–1130, doi:10.1175/JHM-386.1.
- Dugam, S. S., S. B. Kakade, and R. K. Verma, 1997: Interannual and long-term variability in the North Atlantic Oscillation and Indian summer monsoon rainfall. *Theor. Appl. Climatol.*, **58**, 21–29, doi:10.1007/BF00867429.
- Enfield, D. B., A. M. Mestas-Núñez, and P. J. Trimble, 2001: The Atlantic multidecadal oscillation and its relation to rainfall and river flows in the continental U.S. *Geophys. Res. Lett.*, **28**, 2077–2080, doi:10.1029/2000GL012745.
- Evans, M. N., A. Kaplan, M. A. Cane, 2002: Pacific sea surface temperature field reconstruction from coral $d^{18}O$ data using reduced space objective analysis. *Paleoceanography*, **17**, 1007, doi:10.1029/2000PA000590.
- Fang, K., D. Chen, J. Li, and H. Seppä, 2014: Covarying hydroclimate patterns between monsoonal Asia and North America over the past 600 years. *J. Climate*, **27**, 8017–8033, doi:10.1175/JCLI-D-13-00364.1.
- Fowler, H. J., and C. G. Kilsby, 2002: Precipitation and the North Atlantic Oscillation: A study of climatic variability in northern England. *Int. J. Climatol.*, **22**, 843–866, doi:10.1002/joc.765.
- Fye, F. K., D. W. Stahle, E. R. Cook, and M. K. Cleaveland, 2006: NAO influence on sub-decadal moisture variability over central North America. *Geophys. Res. Lett.*, **33**, L15707, doi:10.1029/2006GL026656.
- Griffin, D., and K. J. Anchukaitis, 2014: How unusual is the 2012–2014 California drought? *Geophys. Res. Lett.*, **41**, 9017–9023, doi:10.1002/2014GL026433.
- Guttman, N. B., 1998: Comparing the Palmer drought index and the standardized precipitation index. *J. Amer. Water Resour. Assoc.*, **34**, 113–121, doi:10.1111/j.1752-1688.1998.tb05964.x.
- Harris, I., P. D. Jones, T. J. Osborn, and D. H. Lister, 2014: Updated high-resolution grids of monthly climatic observations—The CRU TS3.10 dataset. *Int. J. Climatol.*, **34**, 623–642, doi:10.1002/joc.3711.
- Heim, R., R. Vose, J. Lawrimore, and E. R. Cook, 2007: Putting current North America drought conditions into a multi-century perspective. Part 2: Using the blended product in operational drought monitoring. *2007 Fall Meeting*, San Francisco, CA, Amer. Geophys. Union, Abstract PP31F-02.
- Hernandez, M., C. C. Ummerhofer, and K. J. Anchukaitis, 2015: Multi-scale drought and ocean–atmosphere variability in monsoon Asia. *Environ. Res. Lett.*, **10**, 074010, doi:10.1088/1748-9326/10/7/074010.
- Herweijer, C., R. Seager, E. R. Cook, and J. Emile-Geay, 2007: North American droughts of the last millennium from a gridded network of tree-ring data. *J. Climate*, **20**, 1353–1376, doi:10.1175/JCLI4042.1.
- Jones, P. D., and A. Moberg, 2003: Hemispheric and large-scale surface air temperature variations: An extensive revision and update to 2001. *J. Climate*, **16**, 206–223, doi:10.1175/1520-0442(2003)016<0206:HALSSA>2.0.CO;2.
- , and Coauthors, 2009: High-resolution palaeoclimatology of the last millennium: A review of current status and future prospects. *Holocene*, **19**, 3–49, doi:10.1177/0959683608098952.
- Karl, T. R., 1986: The sensitivity of the Palmer drought severity index and Palmer's Z-index to their calibration coefficients including potential evapotranspiration. *J. Climate Appl. Meteorol.*, **25**, 77–86, doi:10.1175/1520-0450(1986)025<0077:TSOTPD>2.0.CO;2.
- Krishna Kumar, K., B. Rajagopalan, M. Hoerling, G. Bates, and M. Cane, 2006: Unraveling the mystery of Indian monsoon failure during El Niño. *Science*, **314**, 115–119, doi:10.1126/science.1131152.
- Kushnir, Y., R. Seager, M. Ting, N. Naik, and J. Nakamura, 2010: Mechanisms of tropical Atlantic SST influence on North American precipitation variability. *J. Climate*, **23**, 5610–5628, doi:10.1175/2010JCLI3172.1.
- Livneh, B., and M. P. Hoerling, 2016: The physics of drought in the U.S. central Great Plains. *J. Climate*, **29**, 6783–6804, doi:10.1175/JCLI-D-15-0697.1.
- Mann, M. E., and Coauthors, 2009: Global signatures and dynamical origins of the Little Ice Age and Medieval Climate Anomaly. *Science*, **326**, 1256–1260, doi:10.1126/science.1177303.
- Mares, I., C. Mares, and M. Mihailescu, 2002: NAO impact on the summer moisture variability across Europe. *Phys. Chem. Earth*, **27**, 1013–1017, doi:10.1016/S1474-7065(02)00135-3.
- Masson-Delmotte, V., and Coauthors, 2013: Information from paleoclimate archives. *Climate Change 2013: The Physical Science Basis*. T. F. Stocker et al., Eds., Cambridge University Press, 383–464, doi:10.1017/CBO9781107415324.013.
- McCabe, G. J., and M. D. Dettinger, 2002: Primary modes and predictability of year-to-year snowpack variations in the western United States from teleconnections with Pacific Ocean climate. *J. Hydrometeorol.*, **3**, 13–25, doi:10.1175/1525-7541(2002)003<0013:PMAPOY>2.0.CO;2.
- , M. A. Palecki, and J. L. Betancourt, 2004: Pacific and Atlantic Ocean influences on multidecadal drought frequency in the United States. *Proc. Natl. Acad. Sci. USA*, **101**, 4136–4141, doi:10.1073/pnas.0306738101.
- , J. L. Betancourt, S. T. Gray, M. A. Palecki, and H. G. Hidalgo, 2008: Associations of multi-decadal sea-surface temperature variability with US drought. *Quat. Int.*, **188**, 31–40, doi:10.1016/j.quaint.2007.07.001.
- Mishra, A. K., and V. P. Singh, 2010: A review of drought concepts. *J. Hydrol.*, **391**, 202–216, doi:10.1016/j.jhydrol.2010.07.012.
- Newman, M., G. P. Compo, and M. A. Alexander, 2003: ENSO-forced variability of the Pacific decadal oscillation. *J. Climate*, **16**, 3853–3857, doi:10.1175/1520-0442(2003)016<3853:EVOTPD>2.0.CO;2.
- , and Coauthors, 2016: The Pacific decadal oscillation, revisited. *J. Climate*, **29**, 4399–4427, doi:10.1175/JCLI-D-15-0508.1.
- Nigam, S., B. Guan, and A. Ruiz-Barradas, 2011: Key role of the Atlantic multidecadal oscillation in 20th century drought and wet periods over the Great Plains. *Geophys. Res. Lett.*, **38**, L16713, doi:10.1029/2011GL048650.
- Palmer, J. G., and Coauthors, 2015: Drought variability in the eastern Australia and New Zealand summer drought atlas (ANZDA, CE 1500–2012) modulated by the interdecadal Pacific oscillation. *Environ. Res. Lett.*, **10**, 124002, doi:10.1088/1748-9326/10/12/124002.
- Palmer, W. C., 1965: Meteorological drought. Research Paper No. 45, Weather Bureau, 58 pp.

- Penman, H. L., 1948: Natural evaporation from open water, bare soil and grass. *Proc. Roy. Soc. London*, **193A**, 120–145, doi:10.1098/rspa.1948.0037.
- Phipps, S. J., and Coauthors, 2013: Paleoclimate data–model comparison and the role of climate forcings over the past 1500 years. *J. Climate*, **26**, 6915–6936, doi:10.1175/JCLI-D-12-00108.1.
- Piechota, T. C., and J. A. Dracup, 1996: Drought and regional hydrologic variation in the United States: Associations with the El Niño–Southern Oscillation. *Water Resour. Res.*, **32**, 1359–1373, doi:10.1029/96WR00353.
- Qian, C., and T. Zhou, 2014: Multidecadal variability of north China aridity and its relationship to PDO during 1900–2010. *J. Climate*, **27**, 1210–1222, doi:10.1175/JCLI-D-13-00235.1.
- Routson, C. C., C. A. Woodhouse, and J. T. Overpeck, 2011: Second century megadrought in the Rio Grande headwaters, Colorado: How unusual was medieval drought? *Geophys. Res. Lett.*, **38**, L22703, doi:10.1029/2011GL050015.
- Santer, B. D., K. E. Taylor, T. M. L. Wigley, J. E. Penner, P. D. Jones, and U. Cubasch, 1995: Towards the detection and attribution of an anthropogenic effect on climate. *Climate Dyn.*, **12**, 77–100, doi:10.1007/BF00223722.
- Sarachik, E., and M. A. Cane, 2010: *The El Niño–Southern Oscillation Phenomenon*. Cambridge University Press, 360 pp.
- Schmidt, G. A., and Coauthors, 2014: Using palaeo-climate comparisons to constrain future projections in CMIP5. *Climate Past*, **10**, 221–250, doi:10.5194/cp-10-221-2014.
- Seager, R., R. Burgman, Y. Kushnir, A. Clement, E. R. Cook, N. Naik, and J. Miller, 2008: Tropical Pacific forcing of North American medieval megadroughts: Testing the concept with an atmosphere model forced by coral-reconstructed SSTs. *J. Climate*, **21**, 6175–6190, doi:10.1175/2008JCLI2170.1.
- Smerdon, J. E., A. Kaplan, D. Chang, and M. N. Evans, 2011: A pseudoproxy evaluation of the CCA and RegEM methods for reconstructing climate fields of the last millennium. *J. Climate*, **24**, 1284–1309, doi:10.1175/2010JCLI4110.1.
- , B. I. Cook, E. R. Cook, and R. Seager, 2015: Bridging past and future climate across paleoclimatic reconstructions, observations, and models: A hydroclimate case study. *J. Climate*, **28**, 3212–3231, doi:10.1175/JCLI-D-14-00417.1.
- , and Coauthors, 2017: Comparing proxy and model estimates of hydroclimate variability and change over the Common Era. *Climate Past Discuss.*, doi:10.5194/cp-2017-37, in press.
- Stahle, D. W., F. K. Fye, E. R. Cook, and R. D. Griffin, 2007: Tree-ring reconstructed megadroughts over North America since A.D. 1300. *Climatic Change*, **83**, 133–149, doi:10.1007/s10584-006-9171-x.
- , and Coauthors, 2016: The Mexican Drought Atlas: Tree-ring reconstructions of the soil moisture balance during the late pre-Hispanic, colonial, and modern eras. *Quat. Sci. Rev.*, **149**, 34–60, doi:10.1016/j.quascirev.2016.06.018.
- Stevenson, S., A. Timmermann, Y. Chikamoto, S. Langford, and P. DiNezio, 2015: Stochastically generated North American megadroughts. *J. Climate*, **28**, 1865–1880, doi:10.1175/JCLI-D-13-00689.1.
- , B. L. Otto-Bliesner, and J. T. Fasullo, 2016: “El Niño like” hydroclimate responses to last millennium volcanic eruptions. *J. Climate*, **29**, 2907–2921, doi:10.1175/JCLI-D-15-0239.1.
- St. George, S., D. M. Meko, and E. R. Cook, 2010: The seasonality of precipitation signals embedded within the North American Drought Atlas. *Holocene*, **20**, 983–988, doi:10.1177/0959683610365937.
- Sung, M.-K., W.-T. Kwon, H.-J. Baek, K.-O. Boo, G.-H. Lim, and J.-S. Kug, 2006: A possible impact of the North Atlantic Oscillation on the East Asian summer monsoon precipitation. *Geophys. Res. Lett.*, **33**, L21713, doi:10.1029/2006GL027253.
- Ting, M., Y. Kushnir, R. Seager, and C. Li, 2011: Robust features of Atlantic multi-decadal variability and its climate impacts. *Geophys. Res. Lett.*, **38**, L17705, doi:10.1029/2011GL048712.
- Trigo, R. M., T. J. Osborn, and J. M. Corte-Real, 2002: The North Atlantic Oscillation influence on Europe: Climate impacts and associated physical mechanisms. *Climate Res.*, **20**, 9–17, doi:10.3354/cr020009.
- Ummenhofer, C. C., R. D. D’Arrigo, K. J. Anchukaitis, B. M. Buckley, and E. R. Cook, 2013: Links between Indo-Pacific climate variability and drought in the Monsoon Asia Drought Atlas. *Climate Dyn.*, **40**, 1319–1334, doi:10.1007/s00382-012-1458-1.
- van der Schrier, G., J. Barichivich, K. R. Briffa, and P. D. Jones, 2013: A scPDSI-based global data set of dry and wet spells for 1901–2009. *J. Geophys. Res.*, **118**, 4025–4048, doi:10.1002/jgrd.50355.
- Varikoden, H., J. V. Revadekar, Y. Choudhary, and B. Preethi, 2015: Droughts of Indian summer monsoon associated with El Niño and non-El Niño years. *Int. J. Climatol.*, **35**, 1916–1925, doi:10.1002/joc.4097.
- Warner, R., 2013: *Applied Statistics: From Bivariate through Multivariate Techniques*. 2nd ed. SAGE Publications, 1172 pp.
- Wedgbrow, C. S., R. L. Wilby, H. R. Fox, and G. O’Hare, 2002: Prospects for seasonal forecasting of summer drought and low river flow anomalies in England and Wales. *Int. J. Climatol.*, **22**, 219–236, doi:10.1002/joc.735.
- Wells, N., S. Goddard, and M. J. Hayes, 2004: A self-calibrating Palmer drought severity index. *J. Climate*, **17**, 2335–2351, doi:10.1175/1520-0442(2004)017<2335:ASPDSE>2.0.CO;2.
- Williams, A. P., and Coauthors, 2013: Temperature as a potent driver of regional forest drought stress and tree mortality. *Nat. Climate Change*, **3**, 292–297, doi:10.1038/nclimate1693.
- , R. Seager, J. T. Abatzoglou, B. I. Cook, J. E. Smerdon, and E. R. Cook, 2015: Contributions of anthropogenic warming to California drought during 2012–2014. *Geophys. Res. Lett.*, **42**, 6819–6828, doi:10.1002/2015GL064924.
- Woodhouse, C. A., D. M. Meko, G. M. MacDonald, D. W. Stahle, and E. R. Cook, 2010: A 1,200-year perspective of 21st century drought in southwestern North America. *Proc. Natl. Acad. Sci. USA*, **107**, 21 283–21 288, doi:10.1073/pnas.0911197107.
- Wu, B., T. Zhou, and T. Li, 2009: Seasonally evolving dominant interannual variability modes of East Asian climate. *J. Climate*, **22**, 2992–3005, doi:10.1175/2008JCLI2710.1.
- Wu, R., J. Chen, and W. Chen, 2012: Different types of ENSO influences on the Indian summer monsoon variability. *J. Climate*, **25**, 903–920, doi:10.1175/JCLI-D-11-00039.1.
- Yin, D., M. L. Roderick, G. Leech, F. Sun, and Y. Huang, 2014: The contribution of reduction in evaporative cooling to higher surface air temperatures during drought. *Geophys. Res. Lett.*, **41**, 7891–7897, doi:10.1002/2014GL02039.